

CoTe₂: A quantum critical Dirac metal with strong spin fluctuations

Peter E. Siegfried,^{1,2} Hari Bhandari,^{1,2} Jeanie Qi,³ Rojila Ghimire,⁴ Jayadeep Joshi,^{1,2} Zachary T. Messegee,⁵ Willie Beeson,⁶ Kai Liu,⁶ Madhav Prasad Ghimire,⁴ Yanliu Dang,⁷ Huairuo Zhang,^{7,8} Albert Davydov,⁷ Xiaoyan Tan,⁵ Patrick M. Vora,^{1,2} Igor I. Mazin,^{1,2} and Nirmal J. Ghimire^{1,2,*}

¹*Department of Physics and Astronomy, George Mason University, Fairfax, VA 22030, USA.*

²*Quantum Science and Engineering Center, George Mason University, Fairfax, VA 22030, USA.*

³*Thomas Jefferson High School, Alexandria VA 22312, USA*

⁴*Central Department of Physics, Tribhuvan University, Kirtipur, Kathmandu 44613, Nepal.*

⁵*Department of Chemistry and Biochemistry, George Mason University, Fairfax, Virginia 22030, USA.*

⁶*Physics Department, Georgetown University, Washington, DC 20057, USA.*

⁷*Materials Science and Engineering Division, National Institute of Standards and Technology (NIST), Gaithersburg, Maryland 20899, USA.*

⁸*Theiss Research, Inc., La Jolla, California 92037, USA.*

(Dated: August 30, 2022)

Quantum critical points separating weak ferromagnetic and paramagnetic phases trigger many novel phenomena. Dynamical spin fluctuations not only suppress the long-range order, but can also lead to unusual transport and even superconductivity. Combining quantum criticality with topological electronic properties presents a rare and unique opportunity. Here, by means of ab initio calculations and magnetic, thermal, and transport measurements, we show that the orthorhombic CoTe₂ is close to ferromagnetism, which appears suppressed by spin fluctuations. Calculations and transport measurements reveal nodal Dirac lines, making it a rare combination of proximity to quantum criticality and Dirac topology.

INTRODUCTION

In condensed matter physics, interplay between ionic, electronic, and magnetic degrees of freedom can generate many novel phenomena and quasiparticle excitations. Of particular interest have been topologically protected (i.e., by symmetry) band crossings and other electronic features. The field started with the study of topological insulators, then expanded to semimetals, first to 3D Dirac and Weyl points [1] and even to metals [2–9], leading to unusual magnetotransport properties. The novel physics and rarity of these states, as well as their potential applications [10–12] have been at the forefront of recent research. This said, more often than not it is difficult to see the effect of topologically nontrivial points in metals because they tend to be shadowed by other, trivial parts of the Fermi surface. In this connection, a search has been underway for metals that possess symmetry-driven planes of degeneracy in the momentum space, which can cross the Fermi level and generate continuous nodal lines of Dirac points directly at the Fermi level [13]. Such metals would have a dramatically larger part of the Fermi surface bearing topological phenomena, and thus have potential for more unusual properties such as 3D quantum anomalous Hall effect [5, 14], tunable Weyl points [15], and “drumhead” surface states [16] that are argued to provide a route to higher temperature superconductivity [17].

Coexistence or proximity of such topological states with other exotic phenomena such as non-trivial spin

textures, superconductivity, or quantum criticality can further provide a new route to the properties expected from the interplay of real and momentum space topology, originally discussed in the A-phase of ³He [18, 19]. These promising theoretical proposals have driven and guided recent experimental efforts toward the realization and study of such materials.

Quantum criticality, in particular, zero-temperature magnetic phase transitions, is believed to have connections to several emergent phenomena such as triplet superconductivity [20], non-Fermi liquid scalings [21] and unusual magnetotransport behavior [22]. Some famous examples of such materials are unconventional superconductors (Sr₂RuO₄ and Fe-based superconductors), skyrmionic materials (MnSi and FeSi) and weak itinerant ferromagnet, and superparamagnets (ZrZn₂, Ni₃Al, Ni₃Ga, Pd). As such, a quantum critical system with a substantial presence of topologically-nontrivial states at the Fermi level would provide a novel materials platform for the study of the interplay of real and momentum space topology, but such materials are quite rare.

In this work, we report the synthesis, and magnetic, thermal and magnetotransport properties of single crystal CoTe₂, and argue that it is a quantum critical Dirac metal with Dirac points and multiple nodal lines at the Fermi surface. The material does not show magnetic ordering down to 1.8 K despite the DFT ground state being distinctly ferromagnetic, a hallmark of a magnetic order suppressed by quantum-critical spin fluctuation. We find that CoTe₂ is well described by Moriya’s Self-Consistent Renormalization Theory (SCRT) [23], further supporting the conclusion that CoTe₂ is close to a ferromagnetic quantum critical point. This is highly interesting for its potential for tuning magnetic correlations in the presence

* Corresponding author: nghimire@gmu.edu

of a unique topological electronic behavior.

RESULTS AND DISCUSSION

Single crystals of CoTe_2 were grown using the Te self flux method as described in the Methods section. CoTe_2 has previously been reported in three different space groups [24–26] so the structure of our bulk crystals was verified using multiple complementary methods: powder and single crystal x-ray diffraction, atomic resolved scanning transmission electron microscopy (STEM), and Raman spectroscopy, all confirming the orthorhombic marcasite structure in space group $Pn\bar{m}(\#58)$ [see Supplementary Materials (SM) sections S1 to S3 for a full structural description] [27].

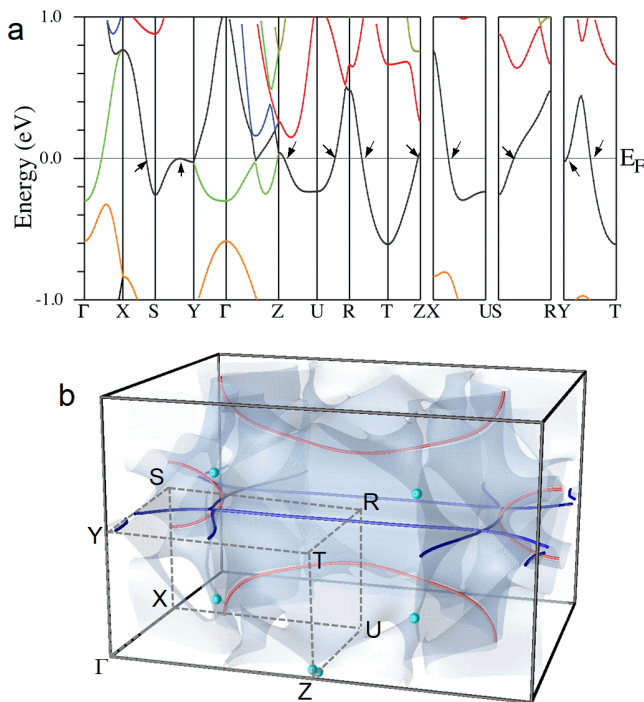


FIG. 1 : (a) Calculated band structure for CoTe_2 . The arrows indicate locations of the Fermi-level Dirac points on these lines, and directions of linear dispersion (see more in SM section S4). (b) The Fermi surface in the first reciprocal lattice cell (from Γ to Γ in all directions) with red and blue tubes showing two types of the Dirac nodal lines and cyan balls indicating Dirac points (except near the top Z point).

We first start by summarizing the electronic band structure of CoTe_2 . Fig. 1 shows the scalar-relativistic (no spin-orbit coupling) band structure along high-symmetry directions and the Fermi surface. The former, depicted in Fig. 1(a), shows a surprisingly large number of degenerate bands, namely along the X-S-Y, Z-U-R-T-Z, X-U, S-R and Y-T lines. To understand this, we recall that CoTe_2 crystallizes in an interesting orthorhombic symmetry, $Pn\bar{m}(\#58)$. This symmetry group is

highly asymmetric: of its 8 symmetry operations half are glide planes. As a result, it has a large number of nodal lines and planes, where all electronic states are doubly degenerate by symmetry. Leonhard *et al.* analyzed all orthorhombic groups [13] and concluded that for this group there are two such planes, defined by the conditions $k_x = \pi/a$ and $k_y = \pi/b$, respectively, and two lines, Z-T and Z-U. Degenerate planes generate nodal lines on the Fermi surface, which in CoTe_2 form two closed loops [shown in Fig. 1(b) as red loops] in the $k_x = \pi/a$ plane and two sets of intersecting infinite lines, plus a small loop around Y (blue) in the $k_y = \pi/b$ one. The two lines identified in Ref. [13] generate two nodal points, shown as two cyan balls near Z in the same figure (note that while these form a quartet of four degenerate points near Z, they do not form, in agreement to the theoretical predictions [13], a closed loop). To the best of our knowledge this is the first direct verification of the Ref. [13]’s predictions for the $Pn\bar{m}$ space group. Note that, in agreement with Ref. [13], the degeneracy is lifted linearly in all directions, providing a large phase space for the Dirac electrons.

In addition, there is a line of *accidental* degeneracy, where two particular bands of Co origin are allowed to cross (without hybridization) in the $k_x = 0$ plane. This line intersects with the Fermi surface at a Dirac point that sits close (but not exactly at) the center of the Γ -Y-T-Z rectangle, and is also shown in Fig. 1(b) by a cyan ball. This Dirac point is 3D (the degeneracy is lifted linearly in all directions) and strongly tilted.

Last but not least, there is one other special Dirac point in the system. From the topological (in classical sense) point of view an isolated Dirac crossing, by definition, only shows degeneracy at one single point in the Brillouin zone, which can only appear on the Fermi level by accident (DP-0). The next level is a nodal line, i.e., a line of Dirac points, which can cross the Fermi surface at isolated points (DP-1). An even stronger, and much less common, there is a nodal plane generating a line of Dirac points on the Fermi level (DP-2). In our case, we have all of those, plus a special Dirac point on the Fermi surface between S and R. Here, the Dirac degeneracy is protected not only when one component of the wave vector is changing (as in DP-1), or two components (DP-2), but all three components k_x , k_y , and k_z (DP-3). Only when two or more components are varied simultaneously, the degeneracy is lifted (see SM section S4 and Figs. S4 and S5 for details). This is the “strongest” Dirac point that can exist in a 3D system, and it occurs rather rarely in real systems.

Often, presence of the Dirac bands near the Fermi surface gives rise to unusual transport signatures. In clean semimetals, they may give rise to extremely large magnetoresistance (MR), quantum oscillations and non-zero Berry phase [28–33] (it is to be noted that the extremely large MR and quantum oscillations in semimetals can have also a non-topological origin [34–36]). However, a combination of multiple Dirac points and lines on the

Fermi surface (coming from nodal lines and planes passing through the entire BZ) have rarely been observed and their manifestation in the transport measurements have not been discussed. To this end, we carried out transport measurements on the single crystals of CoTe₂. Electrical resistivity of CoTe₂ as a function of temperature measured with current (I) along [001] is depicted in Fig. 2(a) (black curve), which shows a metallic character in the entire temperature range between 1.8 and 300 K, consistent with the calculated electronic structure, and does not show any feature indicative of long range magnetic ordering. Specific heat capacity from 1.8 to 200 K is shown in Fig. 2(b) (black curve), which shows a monotonic change with temperature not showing any sign of long range ordering as in the resistivity measurement. Although no long range magnetic ordering is observed in resistivity and heat capacity measurements, their analysis provide information on the average phonon frequency in terms of the Debye temperature, Θ_D . The Debye formula for the specific heat as a function of temperature is

$$C(T) = 9R \left(\frac{T}{\Theta_D} \right)^3 \int_0^{\Theta_D/T} \frac{t^4 e^t}{(e^t - 1)^2} dt + \gamma T, \quad (1)$$

where the first term gives the phonon contribution to the specific heat, and R is the gas constant. The second term is the Sommerfeld electronic specific heat with the coefficient γ giving the mass-renormalized density of states. In the low temperature limit this simplifies to,

$$C(T) = AT^3 + \gamma T. \quad (2)$$

where the first term is the contribution from acoustic phonons, $A = 12\pi^4 R/5\Theta_D^3$. Fitting both the full temperature range to Eq. 1 [red curve in Fig. 2(b)], as well as just the low temperature data to Eq. 2 [inset in Fig. 2(b)] yield similar results finding $\Theta_D = 275.4$ K and $\gamma = 14.22$ mJ·mol⁻¹K⁻¹ for Eq. 1 and $\Theta_D = 273.1$ K and $\gamma = 12.45$ mJ·mol⁻¹K⁻¹ for Eq. 2 and $T < 7$ K, indicating that the contribution from optical phonons at lower temperatures is small. This γ is to be compared with the Sommerfeld coefficient from the unrenormalized DFT density of states, $N(E_F) \approx 6.5$ states/eV·f.u., $\gamma_0 \approx 7.6$ mJ·mol⁻¹K⁻¹, giving a mass renormalization between 60 and 90%; note that if this renormalization were due to electron-phonon coupling the material would have been a good superconductor, so we interpret this as the manifestation of critical spin fluctuations discussed below.

We further analyzed the temperature dependence of the resistivity in terms of the Bloch-Grüneisen (BG) formula[37], where the electrical resistivity is

$$\rho_{xx}(T) = \rho_0 + \rho_{ph}(T) \quad (3)$$

and ρ_0 is the residual resistivity at $T = 0$. The temperature-dependent term is given by[37, 38],

$$\rho_{ph}(T) = \alpha_n \rho_{\Theta_R} \left(\frac{T}{\Theta_R} \right)^n \int_0^{\Theta_R/T} \frac{t^n}{(e^t - 1)(1 - e^{-t})} dt, \quad (4)$$

where α_n is a coefficient describing the scattering rate, Θ_R is the BG temperature, which is typically close, albeit not always equal to the Debye temperature, ρ_{Θ_R} is the residual resistivity at $T = \Theta_R$, and the exponent n takes the value of 2, 3, or 5 depending on the specifics of the electronic interactions present within the material [39–41]. For standard acoustic phonon scattering, the exponent n is 5 and the coefficient α_5 is 4.225. Inserting these values for acoustic phonons as well as fixing the $\Theta_R = \Theta_D$ of 275.4 K, yields a temperature dependent resistivity in close agreement with experiment. It is known that the resistivity can observe a T^2 dependence in the presence of high paramagnetism and large electronic specific heat [41], and further, the assumption that $\Theta_R = \Theta_D$ isn't strictly true [37]. This T^2 dependence would take the same form as Eq. 4, with $n = 2$, and where α_2 is a constant coefficient describing the scattering rate of the T^2 behavior. We find the T^2 dependence at low temperature much more accurately reflects the temperature dependence of resistivity [inset in Fig. 2(a)].

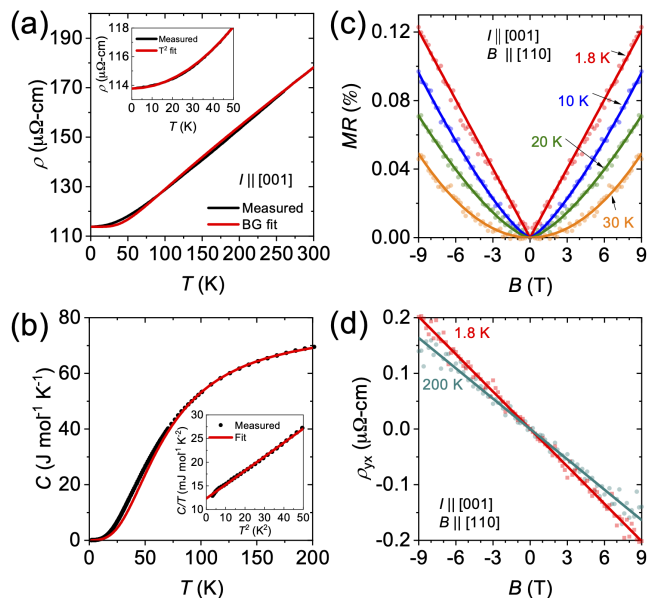


FIG. 2 : (a) Temperature dependence of electrical resistivity (black) and Bloch-Grüneisen fit (red) of CoTe₂ measured with current applied along [001]. Inset shows low-temperature data fitted to $\rho_0 + AT^2$; $\rho_0 = 113.8$ $\mu\Omega\text{-cm}$, and $A = 0.00173$. (b) Specific heat capacity of CoTe₂ as a function of temperature (black) and Debye model fit (Eq. 1, red). The inset shows the measured $T < 7$ K C/T vs T^2 dependence (black) and linear fitting to Eq. 2 (red). (c) Magnetoresistance (MR) of CoTe₂ at indicated temperatures. Solid lines are fits of different functions to the data as described in the text. (d) Hall resistivity vs magnetic field at indicated temperatures. Solid lines are straight line fits to the data.

The magnetoresistance (MR), defined as $[\rho(B) - \rho(B = 0)]/\rho(B = 0)$, for I along [001] and the magnetic field B along [110] between 1.8 and 30 K, is shown in Fig.

2 (c). The MR in CoTe₂ is extremely small but at lower temperatures $T < 10$ K it is linear in magnetic field, and non-saturating. The linear behavior gradually changes with temperature. A $B^{1.31}$ dependence is observed at 10 K, $B^{1.44}$ dependence at 20 K, and finally exhibiting a more conventional B^2 dependence at 30 K. We verified this behavior in more than one samples from different growth batches (see Fig. S6). The linear MR is an interesting property and has been observed in many material systems [42–51]. However, it is frequently observed and used as evidence for materials exhibiting topological features in their electronic structure [42, 43, 47, 49–55]. One prevalent non-topological reason for the linear MR is disorder [45, 46, 53, 56]. But in such a case, the linear MR usually spans a large temperature range unlike the quickly attained quadratic behavior at 30 K in CoTe₂. Another widely observed reason for the linear MR is an admixture of a component of the Hall resistivity (which depends linearly on the magnetic field) to the longitudinal resistance caused by inhomogeneities such as density or sample thickness variations [57]. Such variations give rise to a gradient of the (transverse) Hall voltage in the longitudinal direction that will naturally be picked up in measurements of the longitudinal resistance, therefore giving rise to a linear component in the magnetoresistance. In CoTe₂, the Hall resistivity is linear at all temperatures measured [Fig. 2(d)] and its influence only at the lower temperatures, where the MR is actually larger, is not consistent with this mechanism. In fact, thermal conductivity measured as a function of temperature (see Fig. S7) shows a sharp drop below about 30 K indicating that Umklapp process is frozen out below this temperature and thus the effect of phonon scattering is smaller at the temperature range where linear MR is observed, consistent with the conclusion drawn from the analysis of the heat capacity data. This observation is indicative that with the increase in temperature phonons may play a role in suppressing the linear MR in CoTe₂. As the magnetotransport of such a system with the coexisting nodal points, lines and planes have never been measured and analyzed before, this anomalous magnetotransport behavior of CoTe₂ calls for further theoretical and experimental investigations.

To characterize the magnetism in CoTe₂ we performed DC magnetic measurements. The blue curve in Fig. 3(a) (plotted in the left axis) shows magnetic susceptibility as a function of temperature between 1.8 and 375 K. The susceptibility increases slowly with decreasing temperature but does not show a sign of a long-range ordering, consistent with resistivity and heat capacity measurements. It neither diverges at lower temperatures as in normal paramagnetic materials. It is an indication that the material tends to order but the ordering is somehow suppressed (by strong spin fluctuations, which we will discuss below). Inverse susceptibility after subtracting a small diamagnetic background (χ_0 of -1.58×10^{-5} cm³mol⁻¹F.U.⁻¹) determined from the Curie-Weiss fit to the susceptibility above 50 K (indicated by the red

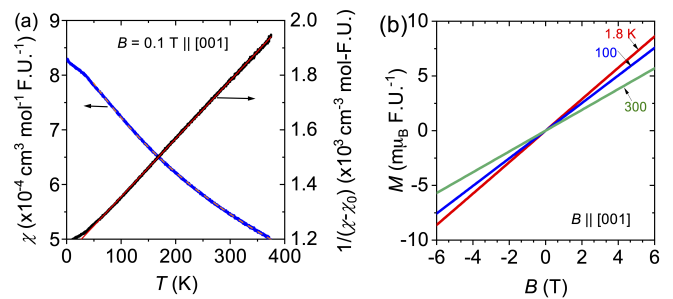


FIG. 3 : (a) DC magnetic susceptibility ($\chi = M/B$) as a function of temperature for $B = 0.1$ T along the c -axis (left axis). The dashed line shows a fit to the Curie-Weiss law between 50 and 375 K, yielding $\chi_0 = -1.585 \times 10^{-5}$ cm³ mol⁻¹ F.U.⁻¹. $1/(\chi - \chi_0)$ vs T is plotted in the right axis (black line). The red solid line is a Curie-Weiss fit. (b) Magnetization vs magnetic field at the indicated temperatures.

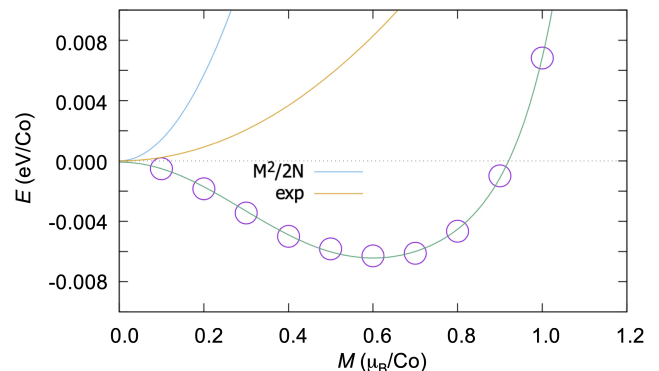


FIG. 4 : DFT calculation predicting a ferromagnetic ground state (purple points). The blue line is the parabola corresponding to the Pauli susceptibility with the calculated density of states N . The orange line is obtained from the Moriya’s SCRT formula with the spin fluctuations amplitude adjusted to match the experimental zero temperature susceptibility (see the text for more details).

dashed line) is plotted in the right hand axis of Fig. 3(a). Thus obtained inverse susceptibility is linear over a wide range of temperature (down to 25 K) and its fitting to the Curie-Weiss law [red solid line in Fig. 3(a)]:

$$1/(\chi - \chi_0) = (T - T_\theta)/C, \quad (5)$$

where χ is the spin susceptibility, C is the Curie constant, and T_θ is the Curie-Weiss temperature, yields the effective moment ($\mu_{\text{eff}} = \sqrt{8C}$) of 1.940 μ_B per Co. This agrees reasonably well with the theoretical μ_{eff} of 1.732 μ_B per Co for the low-spin state ($S = 1/2$) Co⁴⁺. T_θ obtained from the x -intercept is ~ 30 K. The sizable positive value indicates the presence of ferromagnetic correlations. Magnetization data (M vs B) depicted in Fig. 3(b) is linear at all temperatures between 1.8 and 300 K indicating that the paramagnetism observed at room

temperature, unusually, persists down to the lowest measured temperatures. The fact that despite the large T_θ the material does not order down to ~ 1 K indicates strong spin fluctuations.

Additional insight can be gained from the density functional (DFT) calculations. Being mean-field by nature, DFT calculations do not account for fluctuation-driven suppression of magnetic order. Correspondingly, calculating the ferromagnetic total energy in DFT as a function of spin magnetization yields a ferromagnetic ground state with a moment of $M = 0.6\mu_B/\text{Co}$, also corresponding to $S = 1/2$ (with a typical for DFT hybridization reduction), whose total stabilization energy is however only ~ 6 meV/Co, as shown in Fig. 4. The effect of fluctuations can be approximated by means of Moriya's SCRT[23, 58]. If the DFT energy is expanded as a polynomial in M ,

$$E = a + bM^2 + cM^4 + dM^6 + eM^8 \dots, \quad (6)$$

and there are Gaussian fluctuations of the magnetic moment with an average squared amplitude ξ^2 , then, in SCRT, the renormalized energy is given by

$$E = a + (b + 5c\xi^2 + 35d\xi^4 + 35e\xi^6)M^2 + \dots \quad (7)$$

and the renormalized susceptibility is, as usually, $\chi^{-1} = \partial^2 E / \partial M^2$. Typically, Moriya's parameter ξ is comparable with, or somewhat larger than the equilibrium DFT value. Fitting our DFT calculations (the green line in Fig. 4), and assuming fluctuations with $\xi \approx 0.71 \mu_B$, consistent with the DFT moment of $0.6\mu_B$, we can reproduce the experimental susceptibility at $T = 0$. Thus, CoTe₂ is a material where ferromagnetic order is suppressed by strong spin fluctuations, leaving the ground state on the verge of a magnetic quantum critical phase transition.

CONCLUSION

To conclude, our measurements and calculations suggest that CoTe₂ sports a unique combination of a quantum criticality and multiple nodal Dirac lines. The ferromagnetic order is wholly suppressed, maintaining paramagnetic behavior down to the lowest measured temperatures due to strong spin fluctuation. The calculated bands show that this material has potential for harboring new topological physics, as CoTe₂ hosts both nodal Dirac lines, and more conventional Dirac points directly on the Fermi surface, within a single material on the verge of quantum criticality. This study should prompt future investigations into system, for instance, by probing the Dirac dispersions via photoemission and quantum oscillations. A quantum critical point may be reached by doping or pressure to provide further insight into the interplay between magnetism and topological fermions.

METHODS

Single crystal growth and x-ray diffraction.

Single crystals of CoTe₂ were grown by molten metal flux method with Te as a self flux. Co powder (Alfa Aesar; 99.998%), and Te shots (Alfa Aesar; 99.9999%), were loaded in a 2-ml aluminum oxide crucible in a molar ratio of 1:19. The crucible was then sealed in a fused silica ampule under vacuum. The sealed ampule was heated to 800°C over 12 hours, homogenized at 800°C for 10 hours. The furnace was then quickly cooled to 760°C in 2 hours followed by slow cooling to 500°C over 140 hours. Once the furnace reached 500°C, the excess flux was decanted from the crystals using a centrifuge. Well-faceted rectangular crystals as large as 30 mg were obtained. The crystal structure of the compound was first verified by x-ray powder diffraction at room temperature using a Rigaku MiniFlex diffractometer and then by single crystal x-ray diffraction. A few crystals from each growth batch were ground into powder, and x-ray diffraction patterns were collected on those powder samples. Rietveld refinement [59] of powder x-ray pattern was performed using FullProf software [60]. Single-crystal X-ray diffraction data of CoTe₂ were collected on a piece of a representative single crystal at room temperature using a Rigaku XtaLAB Synergy-i diffractometer with the HyPix-Bantam direct photon-counting detector. The single-crystal was glued on a loop and mounted on the goniometer head of the diffractometer. The crystal structure of CoTe₂ was solved with space group $Pn\bar{m}$ and refined with the SHELX program [61].

STEM Measurements. An FEI Helios NanoLab 660 DualBeam (SEM/FIB) system was used to prepare cross-sectional TEM samples. Electron-beam-induced deposition of Pt was initially deposited on top of the materials to protect the sample surface, followed by 3- μm ion-beam induced Pt deposition. To reduce Ga ion damage, 2 kV Ga ion beam was applied to thin the lamella in the final step. An FEI Titan 80-300 STEM/TEM equipped with a probe spherical-aberration corrector was employed to conduct atomic resolved scanning transmission electron microscopy (STEM) imaging.

Raman measurements. Raman measurements of CoTe₂ single crystals were performed at room temperature in a backscattering geometry. The sample was excited by a 532 nm laser focused through a 0.75 NA objective lens with 40 \times magnification. The laser power was measured to be 200 μW before the objective. Scattered light was collected through the same lens and directed to an imaging spectrograph. Rejection of the laser is accomplished using a pair of long pass dielectric filters that allow measurement of Raman scattered light down to 75 cm^{-1} .

Magnetic, transport and thermal measurements. Electronic transport measurements were conducted within the 9-T Quantum Design PPMS with the DC resistivity option. Samples were polished to dimensions of approximately $1.00 \times 0.40 \times 0.12$ mm with the long

axis corresponding to the [001] direction. An excitation current of 4 mA was used for all measurements. Electrical contacts were affixed using Epotek H20E silver epoxy and 25 μm Pt wires with typical contacts resistances of $\approx 10 \Omega$, such that current was directed along the [001] direction. In magnetoresistance measurements, the contact misalignment was corrected by field symmetrizing (for MR) and antisymmetrizing (for Hall) the measured data. Magnetization measurements were made using a Quantum Design VSM SQUID in the field-cooled mode. Heat capacity was measured with the Quantum Design PPMS. The thermal conductivity was measured via the Quantum Design PPMS Thermal Transport Option (TTO) where the sample was polished to a rectangular bar and mounted with the standard TTO thermometer shoes. The sample geometry yielded a cross-sectional area of 0.747 mm^2 with thermometer lead separation of 1.628 mm. The applied heat current was directed along the c-axis of the sample with the heat pulses maintained at 3% of the sample temperature for each temperature setpoint measured.

First-principles Calculations. Most calculations were performed using the all-electron linearized augmented plane wave code WIEN2k[62] with gradient approximation for the exchange-correlation energy[63], including the results shown in Figs. 1 and 3. For control purposes, some calculations were performed using projected augmented wave pseudo-potential code VASP[64]. Fig. S4 was generated using the Full Potential Local Orbitals (FPLO)[65] package (agreement of the results from WIEN2k was verified).

ACKNOWLEDGEMENTS

The authors thank Binghai Yan for insightful discussions. N.J.G acknowledges the support from the NSF CAREER award DMR-2143903. Crystal growth part of the work at George Mason University was supported by the U.S. Department of Energy, Office of Science, Basic Energy Sciences, Materials Science and Engineering Division. I.I.M. acknowledges support from the U.S. Department of Energy through the grant No. DE-SC0021089. M.P.G. acknowledges the Alexander von Humboldt Foundation, Germany and IFW-Dresden, Germany for the equipment grants. R.G. thanks UGC-Nepal for the fellowship with award number MRS-77/78 S & T -119. Magnetic characterization at G.U. have been supported by the NSF (ECCS-2151809). The acquisition of a Magnetic Property Measurements System (MPMS3, Quantum Design) at G.U. used herein was supported by the NSF (DMR-1828420). H.Z. acknowledges support from the U.S. Department of Commerce, NIST under financial assistance award 70NANB19H138. A.D. acknowledges support from the Material Genome Initiative funding allocated to NIST. J.J. and P.M.V. acknowledge support from the NSF CAREER award DMR-1847782.

REFERENCES

-
- [1] N. P. Armitage, E. J. Mele, and A. Vishwanath, Weyl and Dirac semimetals in three-dimensional solids, *Reviews of Modern Physics* **90**, 15001 (2018).
 - [2] A. A. Burkov, M. D. Hook, and L. Balents, Topological nodal semimetals, *Physical Review B* **84**, 235126 (2011).
 - [3] Y. Kim, B. J. Wieder, C. L. Kane, and A. M. Rappe, Dirac Line Nodes in Inversion-Symmetric Crystals, *Physical Review Letters* **115**, 036806 (2015).
 - [4] T. Bzdušek, Q. Wu, A. Rüegg, M. Sgrist, and A. A. Soluyanov, Nodal-chain metals, *Nature* **538**, 75 (2016).
 - [5] J. W. Rhim and Y. B. Kim, Landau level quantization and almost flat modes in three-dimensional semimetals with nodal ring spectra, *Physical Review B* **92**, 045126 (2015), [arXiv:1504.07641](https://arxiv.org/abs/1504.07641).
 - [6] Z. Zhu, G. W. Winkler, Q. Wu, J. Li, and A. A. Soluyanov, Triple Point Topological Metals, *Physical Review X* **6**, 031003 (2016).
 - [7] K.-H. Ahn, W. E. Pickett, and K. W. Lee, Coexistence of Triple Nodal Points, Nodal Links, and Unusual Flat Band in intermetallic APd3 (A=Pb, Sn), *Phys. Rev. B* **98**, 035130 (2018).
 - [8] N. J. Ghimire, M. A. Khan, A. S. Botana, J. S. Jiang, and J. F. Mitchell, Anisotropic angular magnetoresistance and Fermi surface topology of the candidate novel topological metal Pd3Pb, *Physical Review Materials* **2**, 081201(R) (2018).
 - [9] J. F. Houry, A. J. E. Rettie, M. A. Khan, N. J. Ghimire, I. Robredo, J. E. Pfluger, K. Pal, C. Wolverton, A. Bergara, J. S. Jiang, L. M. Schoop, M. G. Vergniory, J. Mitchell, D. Y. Chung, and M. G. Kanatzidis, A new three-dimensional subsulfide Ir2In8 with Dirac semimetal behavior, *Journal of the American Chemical Society* **141**, 19130 (2019).
 - [10] M. J. Gilbert, Topological electronics, *Communications Physics* **4**, 70 (2021).
 - [11] M. M. H. Polash, S. Yalameha, H. Zhou, K. Ahadi, Z. Nourbakhsh, and D. Vashaee, Topological quantum matter to topological phase conversion : Fundamentals , materials , physical systems for phase conversions , and device applications, *Materials Science & Engineering R* **145**, 100620 (2021).
 - [12] N. Kumar, S. N. Guin, K. Manna, C. Shekhar, and C. Felser, Topological Quantum Materials from the Viewpoint of Chemistry, *Chemical Reviews* **121**, 2780 (2021).
 - [13] A. Leonhardt, M. M. Hirschmann, N. Heinsdorf, X. Wu, D. H. Fabiani, and A. P. Schnyder, Symmetry-enforced topological band crossings in orthorhombic crystals : Classification and materials discovery, *Physical Review Materials* **5**, 124202 (2021).

- [14] G. Xu, H. Weng, Z. Wang, X. Dai, and Z. Fang, Chern Semimetal and the Quantized Anomalous Hall Effect in HgCr_2Se_4 , *Physical Review Letters* **107**, 186806 (2011).
- [15] Z. Yan and Z. Wang, Tunable Weyl Points in Periodically Driven Nodal Line Semimetals, *Physical Review Letters* **117**, 087402 (2016).
- [16] G. Bian, T.-r. Chang, R. Sankar, S.-y. Xu, H. Zheng, T. Neupert, C.-k. Chiu, S.-m. Huang, G. Chang, I. Belopolski, D. S. Sanchez, M. Neupane, N. Alidoust, C. Liu, B. Wang, C.-c. Lee, H.-t. Jeng, C. Zhang, Z. Yuan, S. Jia, A. Bansil, F. Chou, H. Lin, and M. Z. Hasan, Topological nodal-line fermions in spin-orbit metal PbTaSe_2 , *Nature Communications* **7**, 10556 (2016).
- [17] N. B. Kopnin, T. T. Heikkil, and G. E. Volovik, High-temperature surface superconductivity in topological flat-band systems, *Physical Review B* **83**, 220503 (2011).
- [18] G. E. Volovik, *The Universe in a Helium Droplet* (Oxford University Press, Oxford, 2012).
- [19] G. E. Volovik, Quantum Phase Transitions from Topology., in *Momentum Space in Quantum Analogues: From Phase Transitions to Black Holes and Cosmology, Lecture Notes in Physics*, edited by W. G. Unruh and R. Schützhold (Springer, Berlin Heidelberg, 2007) pp. 31–73.
- [20] D. J. Singh and I. I. Mazin, Competition of Spin Fluctuations and Phonons in Superconductivity of ZrZn_2 , *Physical Review Letters* **88**, 187004 (2002).
- [21] J. R. Stewart, B. D. Rainford, R. S. Eccleston, and R. Cywinski, Non-Fermi-Liquid Behavior of Electron-Spin Fluctuations in an Elemental Paramagnet, *Physical Review Letters* **89**, 186403 (2002).
- [22] I. I. Mazin, D. J. Singh, and A. Aguayo, Density functional calculations near ferromagnetic quantum critical points, in *Physics of Spin in Solids: Materials, Methods and Applications* (Springer, Dordrecht, 2004) pp. 139–154.
- [23] T. Moriya, *Spin Fluctuations in Itinerant Electron Magnetism* (Springer, Verlag, Berlin, Heidelberg, New-York, 1985).
- [24] G. Brostigen and A. Kjekshus, Compounds with Marcasite Type Crystal Structure V. The crystal structure of FeS_2 , FeTe_2 , and CoTe_2 , *Acta Chemica Scandinavica* **24**, 1925 (1970).
- [25] J. A. R. Cheda, E. F. Westrum, and F. Gronvold, Heat Capacity and Other Thermodynamic Properties of CoTe_2 from 5 to 1030 K and of CoTe_2 . 315 from 300 to 1040 K, *Monatshefte für Chemie* **117**, 1223 (1986).
- [26] H. Ma, W. Dang, X. Yang, B. Li, Z. Zhang, P. Chen, Y. Liu, Z. Wan, Q. Qian, J. Luo, K. Zang, X. Duan, and X. Duan, Chemical Vapor Deposition Growth of Single Crystalline CoTe_2 Nanosheets with Tunable Thickness and Electronic Properties, *Chemistry of Materials* **30**, 8891 (2018).
- [27] NIST disclaimer: Certain commercial equipment, instruments, or materials are identified in this paper in order to specify the experimental procedure adequately. Such identifications are not intended to imply recommendation or endorsement by the National Institute of Standards and Technology (NIST), nor it is intended to imply that the materials or equipment identified are necessarily the best available for the purpose.
- [28] M. N. Ali, J. Xiong, S. Flynn, J. Tao, Q. D. Gibson, L. M. Schoop, T. Liang, N. Haldolaarachchige, M. Hirschberger, N. P. Ong, and R. J. Cava, Large, non-saturating magnetoresistance in WTe_2 , *Nature* **514**, 205 (2014).
- [29] N. J. Ghimire, Y. Luo, M. Neupane, D. J. Williams, E. D. Bauer, and F. Ronning, Magnetotransport of single crystalline NbAs, *Journal of Physics: Condensed Matter* **27**, 152201.
- [30] T. Liang, Q. Gibson, M. N. Ali, M. Liu, R. J. Cava, and N. P. Ong, Ultrahigh mobility and giant magnetoresistance in the Dirac semimetal Cd_3As_2 , *Nature Materials* **14**, 280 (2015), arXiv:1404.7794.
- [31] N. J. Ghimire, A. S. Botana, D. Phelan, H. Zheng, and J. F. Mitchell, Magnetotransport of single crystalline YSb, *Journal of Physics Condensed Matter* **28**, 19 (2016).
- [32] A. A. Burkov, Anomalous Hall Effect in Weyl Metals, *Phys. Rev. Lett.* **113**, 187202 (2014).
- [33] M. H., B. M.S., T. M., K. Y., B. C., K. Y., N. N., H. H. Y., and T. Y., Detection of Berry's Phase in a Bulk Rashba Semiconductor, *Science* **342**, 1490 (2013).
- [34] Y. Luo, R. D. McDonald, P. F. Rosa, B. Scott, N. Wakeham, N. J. Ghimire, E. D. Bauer, J. D. Thompson, and F. Ronning, Anomalous electronic structure and magnetoresistance in TaAs_2 , *Scientific Reports* **6**, 27294 (2016).
- [35] S. Sun, Q. Wang, P.-J. Guo, K. Liu, and H. Lei, Large magnetoresistance in LaBi: origin of field-induced resistivity upturn and plateau in compensated semimetals, *New Journal of Physics* **18**, 082002 (2016), arXiv:1601.04618.
- [36] J. He, C. Zhang, N. J. Ghimire, T. Liang, C. Jia, J. Jiang, S. Tang, S. Chen, Y. He, S. K. Mo, C. C. Hwang, M. Hashimoto, D. H. Lu, B. Moritz, T. P. Devereaux, Y. L. Chen, J. F. Mitchell, and Z. X. Shen, Distinct Electronic Structure for the Extreme Magnetoresistance in YSb, *Physical Review Letters* **117**, 267201 (2016).
- [37] J. M. Ziman, *Electrons and Phonons: The Theory of Transport Phenomena in Solids* (Oxford University Press, 2001) reprint ed.
- [38] A. Bid, A. Bora, and A. K. Raychaudhuri, Temperature dependence of the resistance of metallic nanowires of diameter $D = 15$ nm: Applicability of Bloch-Grüneisen theorem, *Physical Review B* **74**, 035426 (2006).
- [39] D. Cvijovic, The Bloch – Grüneisen function of arbitrary order and its series representations, *Theoretical and Mathematical Physics* **166**, 37 (2011).
- [40] A. H. Wilson, The electrical conductivity of the transition metals, *Proc. R. Soc. Lond. A* **157**, 580 (1938).
- [41] W. G. Barber, The contribution of the electrical resistance of metals from collisions between electrons, *Proc. R. Soc. Lond. A* **158**, 383 (1937).
- [42] W. Zhang, R. Yu, W. Feng, Y. Yao, H. Weng, X. Dai, and Z. Fang, Topological Aspect and Quantum Magnetoresistance of β - Ag_2Te , *Physical Review Letters* **106**, 156808 (2011).
- [43] C. M. Wang and X. L. Lei, Linear magnetoresistance on the topological surface, *Physical Review B* **86**, 035442 (2012).
- [44] T. Khouri, U. Zeitler, C. Reichl, W. Wegscheider, N. E. Hussey, S. Wiedmann, and J. C. Maan, Linear Magnetoresistance in a Quasifree Two-Dimensional Electron Gas in an Ultrahigh Mobility GaAs Quantum Well, *Phys. Rev. Lett.* **117**, 256601 (2016).
- [45] N. V. Kozlova, N. Mori, O. Makarovskiy, L. Eaves, Q. D. Zhuang, A. Krier, and A. Patané, Linear magnetoresistance due to multiple- electron scattering by low-mobility islands in an inhomogeneous conductor, *Nature Commu-*

- nications **3**, 1097 (2012).
- [46] R. Xu, A. Husmann, T. F. Rosenbaum, M.-L. Saboungi, J. E. Enderby, and P. B. Littlewood, Large magnetoresistance in non-magnetic silver chalcogenides, *Nature* **390**, 57 (1997).
- [47] Y. Zhao, H. Liu, J. Yan, W. An, J. Liu, X. Zhang, H. Wang, Y. Liu, H. Jiang, Q. Li, Y. Wang, X.-z. Li, D. Mandrus, X. C. Xie, M. Pan, and J. Wang, Anisotropic magnetotransport and exotic longitudinal linear magnetoresistance in WTe₂ crystals, *Physical Review B* **92**, 041104 (2015).
- [48] J. Feng, Y. Pang, D. Wu, Z. Wang, H. Weng, J. Li, X. Dai, Z. Fang, Y. Shi, and L. Lu, Large linear magnetoresistance in Dirac semimetal Cd₃As₂ with Fermi surfaces close to the Dirac points, *Physical Review B* **92**, 081306(R) (2015).
- [49] M. Novak, S. Sasaki, K. Segawa, and Y. Ando, Large linear magnetoresistance in the Dirac semimetal TlBiSSe, *Phys. Rev. B* **91**, 041203(R) (2015).
- [50] H. Tang, D. Liang, R. L. J. Qiu, and X. P. A. Gao, Linear Magneto-Resistance in Topological Insulator Bi₂Se₃ Nanoribbons, *ACS nano* **5**, 7510 (2011).
- [51] G. M. Gusev, E. B. Olshanetsky, Z. D. Kvon, N. N. Mikhailov, and S. A. Dvoretzky, Linear magnetoresistance in HgTe quantum wells, *Phys. Rev. B* **87**, 081311(R) (2013).
- [52] A. A. Abrikosov, Quantum magnetoresistance, *Phys. Rev. B* **58**, 2788 (1998).
- [53] J. Hu and T. F. Rosenbaum, Classical and quantum routes to linear magnetoresistance, *Nature* **7**, 697 (2008).
- [54] C. Fang, Y. Chen, H.-y. Kee, and L. Fu, Topological nodal line semimetals with and without spin-orbital coupling, *Physical Review B* **92**, 081201 (2015).
- [55] I. A. Leahy, Y.-p. Lin, P. E. Siegfried, A. C. Treglia, J. C. W. Song, R. M. Nandkishore, and M. Lee, Non-saturating large magnetoresistance in semimetals, *PNAS* **115**, 10570 (2018).
- [56] M. M. Parish and P. B. Littlewood, Non-saturating magnetoresistance in heavily disordered semiconductors, *Nature* **426**, 162 (2003).
- [57] G. J. C. L. Bruls, J. Bass, A. P. van Gelder, H. van Kempen, and P. Wyder, Linear Magnetoresistance Caused by Sample Thickness Variations, *Physical Review Letters* **46**, 553 (1981).
- [58] P. Larson, I. I. Mazin, and D. J. Singh, Magnetism, critical fluctuations, and susceptibility renormalization in Pd, *Phys. Rev. B* **69**, 064429 (2004).
- [59] L. B. McCusker, R. B. Von Dreele, D. E. Cox, D. Louër, and P. Scardi, Rietveld refinement guidelines, *J. Appl. Cryst.* **32**, 36 (1999).
- [60] J. Rodriguez-carvajal, Recent advances in magnetic structure determination by neutron powder diffraction, *Physica B* **192**, 55 (1993).
- [61] G. M. Sheldrick, A short history of SHELX, *Acta Crystallographica A* **64**, 112 (2008).
- [62] P. Blaha and E. al., *An Augmented Plane Wave Plus Local Orbitals Program for Calculating Crystal Properties* (Vienna University of Technology, Austria, 2001) p. (Austria: Vienna University of Technology).
- [63] J. P. Perdew, K. Burke, and M. Ernzerhof, Generalized gradient approximation made simple, *Physical Review Letters* **77**, 3865 (1996), arXiv:0927-0256(96)00008 [10.1016].
- [64] G. Kresse and J. Furthmüller, Efficient iterative schemes for ab initio total-energy calculations using a plane-wave basis set, *Physical Review B* **54**, 11169 (1996).
- [65] K. Koepnik and H. Eschrig, Full-potential nonorthogonal local-orbital minimum-basis band-structure scheme, *Physical Review B* **59**, 1743 (1999).
-

Supplementary Information for:

CoTe₂: A quantum critical Dirac metal with strong spin fluctuations

Peter E. Siegfried, Hari Bhandari, Jeanie Qi, Rojila Ghimire, Jayadeep Joshi, Zachary T. Messeguee, Willie Beeson, Kai Liu, Madhav Prasad Ghimire, Yanliu Dang, Huairuo Zhang, Albert Davydov, Xiaoyan Tan, Patrick M. Vora, Igor I. Mazin, and Nirmal J. Ghimire

S1. X-RAY DIFFRACTION

TABLE S1 : Structure Refinement Parameters, Atomic Coordinates and Anisotropic Thermal Parameters for CoTe₂.

Formula	CoTe ₂				
Crystal system	Orthorhombic				
Temperature (K)	293				
λ (Å)	0.71073				
Space group	<i>Pnmm</i>				
Unit cell a, b, c (Å)	5.3176(10), 6.3186(2), 3.8864(10)				
V , (Å ³)	130.582(6)				
Z	2				
Crystal size (mm ³)	0.082, 0.126, 0.065				
ρ_{calc} , g cm ⁻³	7.989				
μ , mm ⁻¹	28.074				
θ_{max} , deg	36.265				
Reflections collected	2277				
R_{int}	0.0286				
Unique reflections	357				
Parameters refined	12				
R_1, wR_2 [$F_0 > 4\sigma(F_0)$]	0.0278, 0.0751				
Diff. peak and hole, e (Å ⁻³)	2.227, -3.577				
Goodness-of-fit	1.192				
Atom	Wyck.Site	x	y	z	Occupancy
Co	$2a$	0	0	0	1.00
Te	$4g$	0.21949(6)	0.36340(5)	0	1.00
U_{11} (Å ²)	U_{22} (Å ²)	U_{33} (Å ²)	U_{23} (Å ²)	U_{13} (Å ²)	U_{12} (Å ²)
0.0094(4)	0.0077(4)	0.0091(4)	0	0	-0.0002(3)
0.0064(2)	0.0057(2)	0.0075(2)	0	0	-0.00073(7)

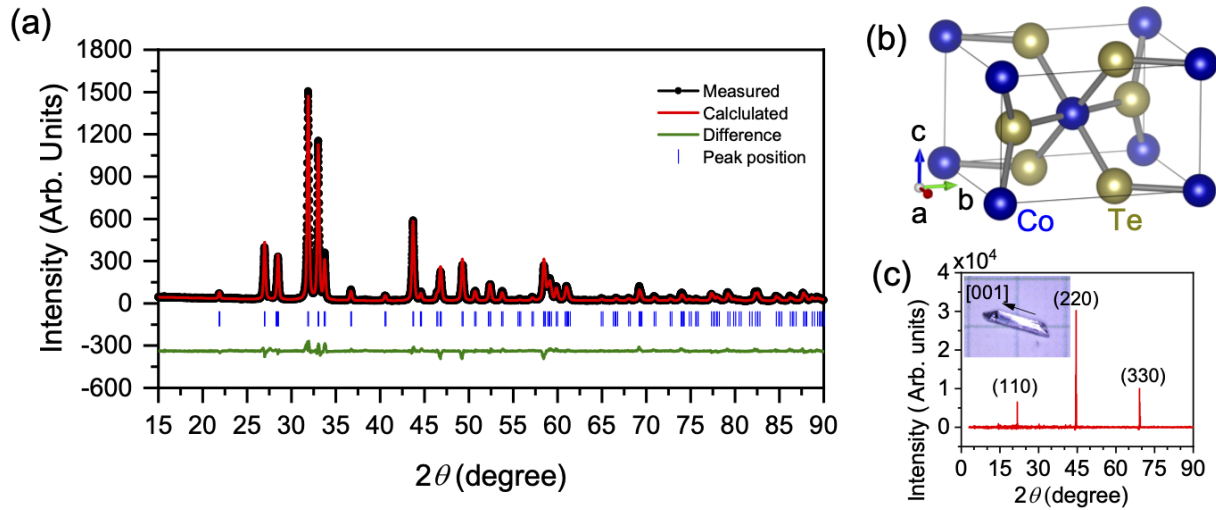


FIG. S1 : a) Rietveld refinement of x-ray powder pattern of CoTe_2 collected at room temperature. b) Crystal structure of CoTe_2 . c) $(hk0)$ x-ray peaks obtained from the as-grown flat face of a single crystal of CoTe_2 as shown in the inset. The $[001]$ direction is along the length of the crystal as indicated by the arrow in the inset.

S2. STEM MEASUREMENTS

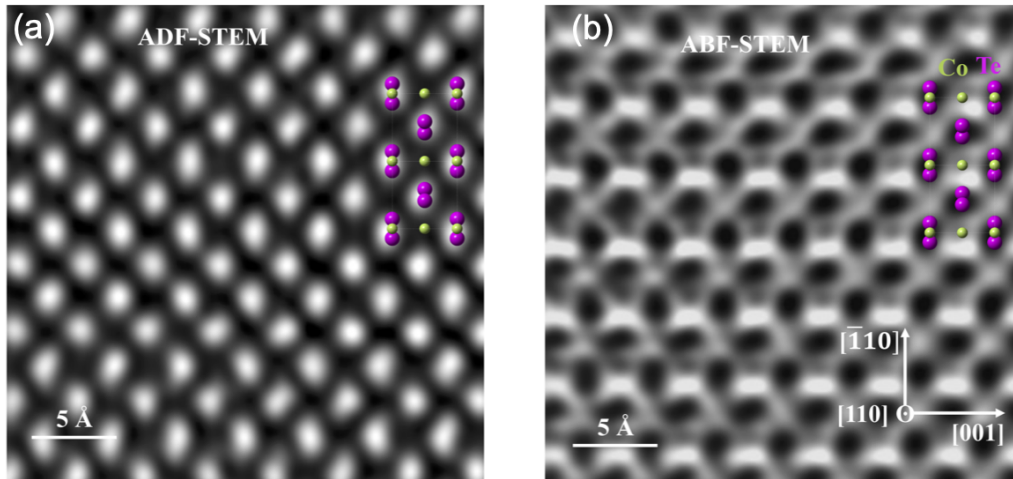


FIG. S2 : Scanning transmission electron microscopy (STEM) images of CoTe_2 . (a) Annular dark-field STEM image. (b) Annular bright-field STEM image.

Figure S2 shows the atomic resolved annular dark-field (ADF) and annular bright-field (ABF) STEM images which were taken simultaneously along the $[110]$ zone-axis. The inserted atomic model of CoTe_2 with the $Pn\bar{m}$ space group matches well with the atomic images.

S3. RAMAN MEASUREMENTS

Raman spectrum of CoTe_2 is presented in Fig. S3. The phonon mode frequencies are determined by fitting the data to a sum of three Lorentzians. The spectrum is dominated by two modes at 122.79 cm^{-1} and 142.41 cm^{-1} to

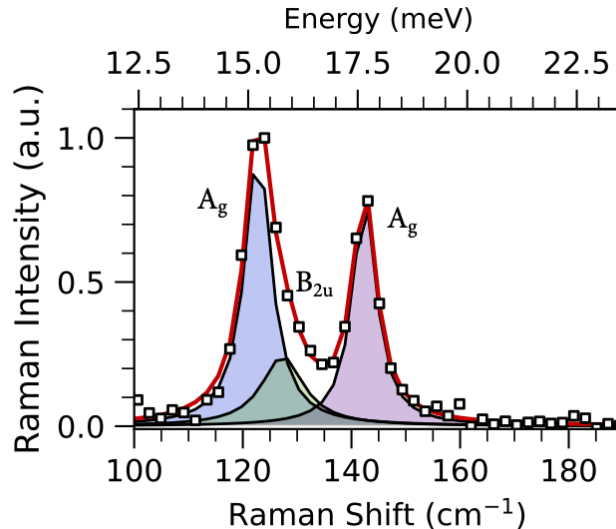


FIG. S3 : Room temperature CoTe₂ Raman spectrum (squares) fit with the sum of three Lorentzian functions (red line). Individual Lorentzians comprising the fit are shaded in blue, green, and purple.

which we assign A_g symmetry based on our DFT calculations (Table S2). There is additional spectral weight between these two modes that can be accounted for with a third Lorentzian centered at 127.32 cm^{-1} . While no Raman active modes are expected here, DFT calculations do predict a mode of B_{2u} symmetry. We therefore suggest this feature is a B_{2u} symmetry mode activated by disorder.

TABLE S2 : Experimental and Theoretical Phonon Frequencies Determined from Fits to the Raman Spectrum in Figure S3 and DFT Calculations, Respectively.

Experiment		DFT Calculation	
Mode Frequency (cm^{-1})	Symmetry	Mode Frequency (cm^{-1})	Symmetry
122.79 ± 0.15	A_g	127.4524 ± 0.9480	A_g
127.32 ± 1.43	B_{2u}	130.7357 ± 0.6270	B_{2u}
142.41 ± 0.08	A_g	144.7070 ± 0.0288	A_g

S4. FIRST-PRINCIPLES CALCULATIONS

Figure S4(a) shows the band structure calculated with (red lines) and without (blue lines) spin-orbit coupling (SOC) [the latter is the same as the one presented in Fig. 1(a) in the main text]. Bands along the maximum-splitting directions are shown in Figs. S4(b-k) from the corresponding points labelled as b-k in Panel (a) showing how the band degeneracy is lifted when moved away from these points forming the nodal lines at the Fermi surface depicted by the red and blue lines in Fig. 1(b) in the main text. It is to be noted that the Dirac point between S and R labelled by i, j in Panel (a) is a special point where the bands remain degenerate along k_x , k_y , and k_z as shown in Fig. S4(i) (moving along k_y ; same behavior is observed moving along k_x , and k_z that are not shown here). The degeneracy is lifted in-between as shown by a representative plot calculated from $(0.3, 0.5, 0.14)$ to $(0, 0, 0.25)$ and schematically illustrated by the four-fold symmetry in Fig. S5. The Dirac points b, c and i in Fig. S4(a) [see Figs. S4(b, c and i)] are symmetry protected and do not open gap with SOC, consistent with the prediction of ref. 13. SOC opens gaps at all other Dirac points indicated in Fig. S4(a) [see Figs. S4(d, e, f, g, h, j, and k)].

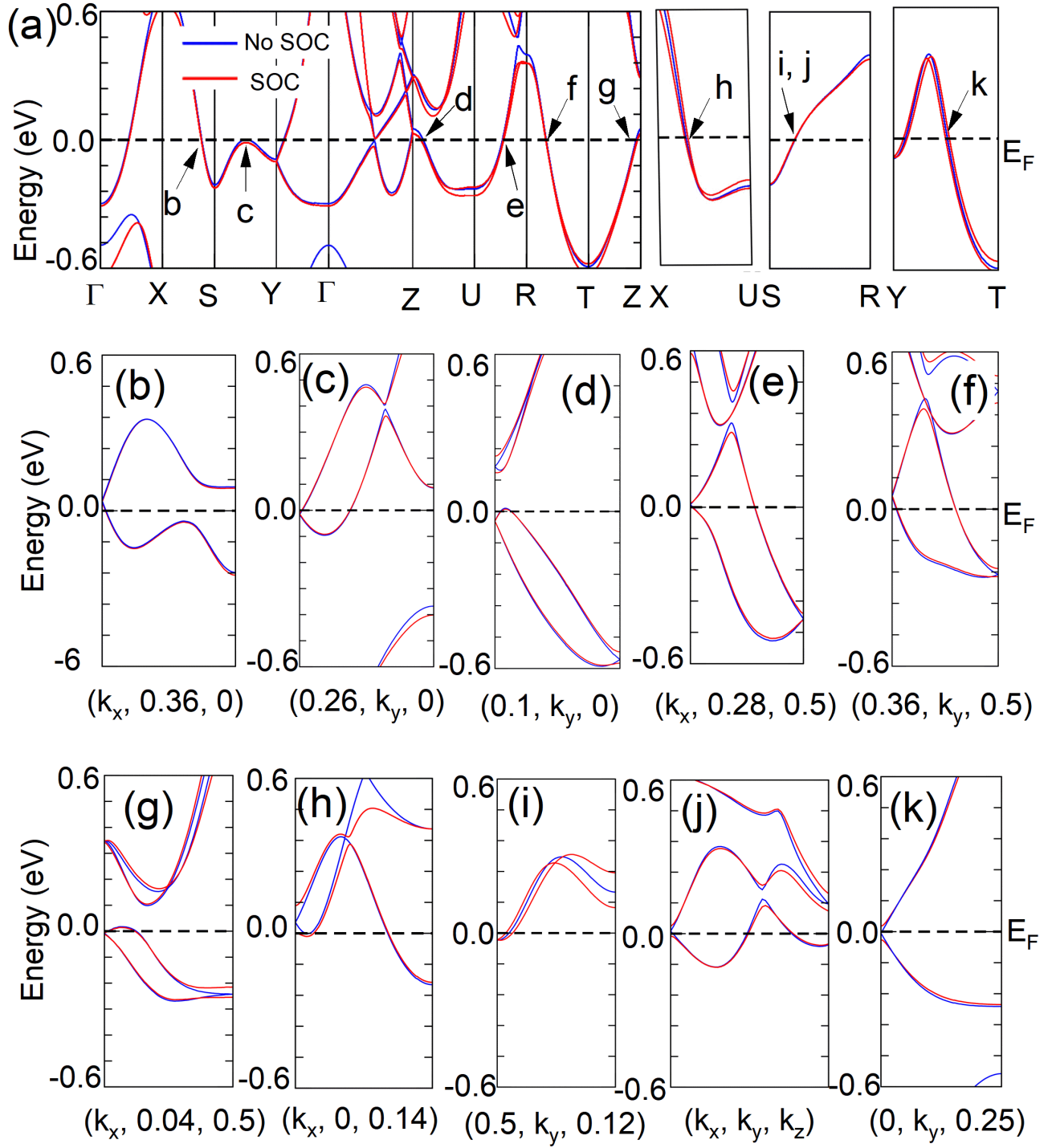


FIG. S4 : (a) Band Structures of CoTe₂ without SOC (blue) and with SOC (red). (b-k) Bands along k_x , k_y , and k_z from the Dirac points indicated by letters b to k in panel (a) showing the lifting of degeneracy along the directions as indicated. Point i in panel (a) is a special point where the degeneracy is protected along k_x , k_y , and k_z [variation along k_y is shown in panel (i)], and lifted in between as shown in panel (j) where all k_x , k_y , and k_z are varied simultaneously.

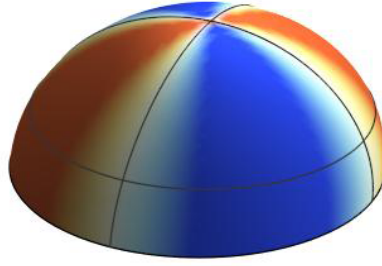


FIG. S5 : Schematic of the degeneracy of Dirac points along SR [see Fig. S4(a)]. The degeneracy is protected along k_x , k_y , and k_z , but lifted at other points showing a four-fold degeneracy-lifting pattern. The diagram shows a patch of the Fermi surface around the point (top of the figure) where it intersects with the SR line (vertical in the cartoon). The color intensity represents the amplitude of the Dirac splitting, and different colors indicate that the band character is swapped by crossing a nodal line.

S5. MAGNETORESISTANCE AND THERMAL CONDUCTIVITY

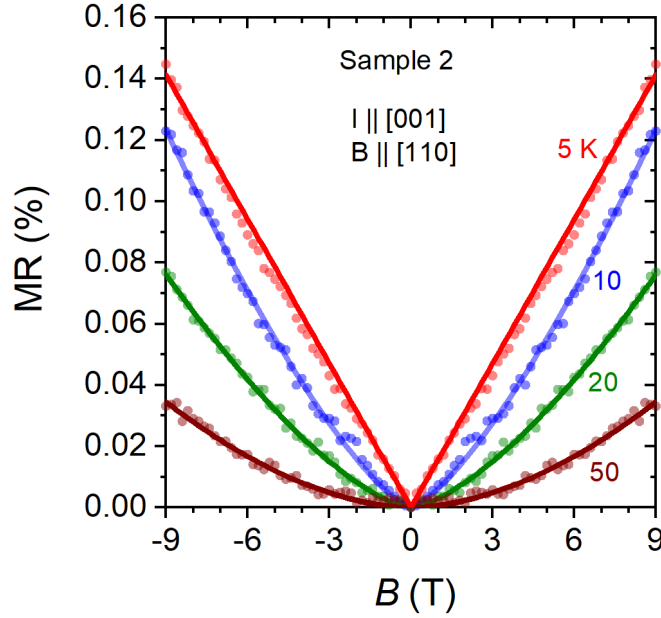


FIG. S6 : Magnetoresistance of a second sample from a growth batch different from that shown in Fig. 2(c) of the main text showing the linear MR at 5 K, which gradually deviates from the linear behavior. The solid spheres are the measured data, and the solid lines are B^n fits to the measured data, where B is the magnetic field. At 5 K, $n = 1$ which gradually increases toward 2 with the increase in temperature.

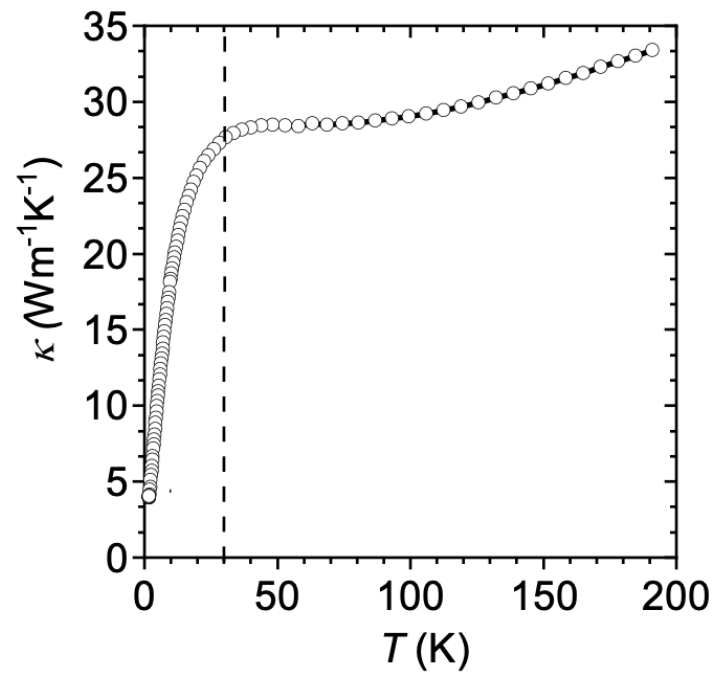


FIG. S7 : Thermal conductivity (κ) of CoTe₂ as a function of temperature. The dashed vertical line is a guide to eye for $T = 30$ K.